

## Double dual-nodal-line semimetals with large surface density of states: Topological quantum catalysts for the hydrogen-evolution reaction

Xiaotian Wang<sup>1,2,§</sup>, Lirong Wang<sup>3,§</sup>, Chengwu Xie<sup>4,§</sup>, Ying Liu<sup>3</sup>, Guodong Liu<sup>3</sup>, Wenhong Wang<sup>4</sup>, Zhenxiang Cheng<sup>2,\*</sup>, Gang Zhang<sup>5,†</sup>, and Xiaoming Zhang<sup>3,‡</sup>

<sup>1</sup> School of Physical Science and Technology, Southwest University, Chongqing 400715, China

<sup>2</sup> Institute for Superconducting and Electronic Materials (ISEM), University of Wollongong, Wollongong 2500, Australia

<sup>3</sup> State Key Laboratory of Reliability and Intelligence of Electrical Equipment, and School of Materials Science and Engineering, Hebei University of Technology, Tianjin 300130, China

<sup>4</sup> School of Electronics & Information Engineering, Tiangong University, Tianjin 300387, China

<sup>5</sup> Institute of High-Performance Computing, Agency for Science, Technology, and Research (A\*STAR), 138632, Singapore



(Received 21 July 2023; revised 10 September 2023; accepted 25 September 2023; published 17 October 2023)

Topological quantum catalysts are developing rapidly due to the emergence of exotic quantum materials and their corresponding catalytic performance. Although tens of thousands of topological semimetals have been developed, their low topological surface density of states (DOSs) remains a hindrance to the development of high-performance catalysts for electrochemical hydrogen evolution reactions (HERs). In this work, we investigate the potential of double dual-nodal line (DDNL) semimetals, which exhibit large surface DOSs and fair-low Gibbs free energies, as ideal topological quantum catalysts (TQCs) for HER. Using the NaAlGe compound as a representative example, we demonstrate that its DDNLs and high surface DOSs around the Fermi level provide advantages for achieving exceptionally high catalytic activity in the electrochemical HER process. Through a comparison of catalytic performance under different (electron and hole) doping and uniaxial strain conditions, we establish a linear correlation between the Gibbs free energy ( $\Delta G_{H^*}$ ) and the projected surface DOSs on the (001) semi-infinite surface of the DDNL semimetal NaAlGe, specifically for the hydrogen evolution process. Our work introduces an alternative category of high-performance TQCs free of noble metals and contributes to a better understanding of the relationship between catalytic performance for HER and surface DOSs in DDNL semimetals.

DOI: 10.1103/PhysRevApplied.20.044042

### I. INTRODUCTION

The excessive utilization of fossil fuels has resulted in significant environmental pollution issues. Hydrogen [1–3], being a renewable energy source that does not generate greenhouse emissions, can effectively address the problem of atmospheric pollution. Water electrolysis is an efficient method for hydrogen production, wherein a substantial amount of hydrogen is generated at the cathode through the reaction  $(2H^+ + 2e^- \rightarrow H_2)$ . However, a major drawback of water electrolysis for hydrogen production is its high electrical energy requirement. To enhance hydrogen production efficiency, it becomes necessary to explore electrocatalysts with low chemical potential [4–10]. The

noble metal Pt [11] has been established as the most effective electrocatalyst for hydrogen production. Nevertheless, its expensive cost and limited availability hinder its large-scale industrial application. Therefore, the pursuit of noble-metal-free, highly effective catalysts for HER has gained considerable attention. Fortunately, topological materials offer an ideal platform for the design of high-performance catalysts. Due to their highly conductive and robust projected surface states, topological materials have recently been identified as prime candidates for catalysts, known as topological quantum catalysts (TQCs) [12,13], in a variety of reactions. Initially, topological insulators were targeted as the primary materials for TQCs [14–16], as their nontrivial band topology in bulk induces highly active states on specific surfaces, thereby facilitating the catalytic process for diverse reactions. For instance, the robust topological surface states (TSSs) of gold-coated  $Bi_2Se_3$  [14] were found to enhance CO oxidation by increasing the adsorption energy of both CO and  $O_2$  molecules through

\*cheng@uow.edu.au

†zhanggg@ihpc.a-star.edu.sg

‡zhangxiaoming87@hebut.edu.cn

§These authors contributed equally to this work.

the promotion of distinct directions of static electron transfer. Subsequently, investigations on TQCs extended from topological insulators to topological semimetals [17–25]. Different types of topological semimetals, including Weyl semimetals [17,18], Dirac semimetals [19], multifold degenerate nodal-point semimetals [20,21], and nodal-line semimetals [22–25], have been reported as potential TQCs capable of significantly improving the HER performance based on experimental and theoretical evidence. Notably, in 2023, Meng *et al.* [21] predicted that the presence of multifold (fourfold and sixfold) degenerate nodal points with extensive arc-shaped TSSs in the electride  $12\text{CaO} \cdot 7\text{Al}_2\text{O}_3$  would enhance its catalytic efficacy for the HER process. They further established a linear relationship between catalytic enhancement and the length of the arc-shaped surface states, providing direct evidence that catalytic enhancement stems from TSSs.

In TQCs, the remarkable catalytic performance primarily stems from the presence of highly surface carrier-dense TSSs [23], which effectively facilitate the catalytic process by providing potential active sites. In addition, TSSs are typically protected by specific symmetry and bulk topology, rendering them robust against perturbations. As a result, the topological surface DOSs proximity to the Fermi level serves as a key determinant of the catalytic efficacy of TQCs in most scenarios. Put simply, the higher the surface DOSs around the Fermi level, the greater the catalytic performance for HER in various TQCs.

In this work, we demonstrate that DDNL semimetals [26] with higher surface DOSs than previously postulated TQCs, including Weyl semimetals and single nodal-line semimetals, can be an ideal HER platform. Using the DDNL semimetal NaAlGe as our prime example [27,28], we showcase its suitability as an ideal candidate for a noble metal-free HER catalyst. NaAlGe exhibits high surface DOSs around the Fermi level on the (001) surface,

coupled with near to zero  $\Delta G_{\text{H}^*}$ , resulting in remarkable catalytic activity for the HER process. To strengthen our findings, we also calculated  $\Delta G_{\text{H}^*}$  and the corresponding surface DOSs of the Fermi level for the other surfaces (010, 101, 110, 210, and 310), successfully establishing a linear relationship between  $\Delta G_{\text{H}^*}$  and surface DOSs. In addition, we introduced various (electron and hole) doping and uniaxial strain conditions to manipulate the values of the surface DOSs of the Fermi level on the (001) semi-infinite surface. Interestingly, our observation revealed a consistent linear correlation between  $\Delta G_{\text{H}^*}$  and projected surface DOSs. These significant findings highlight that topological semimetals with DDNLs are promising platforms for developing HER catalysts. Alongside NaAlGe, we identify four additional candidates, namely NaAlSi, ErSe<sub>2</sub>, NaZnSb, and BaAlGeF, as ideal TQCs with DDNLs and favorable Gibbs free energies ranging from 0.01 to 0.12 eV for HER.

## II. CONCEPTUAL DESIGN

In previous studies [21–25], considerable effort has been dedicated to investigating the role of TSSs in the catalytic enhancement of TQCs. Liu *et al.* [29], for instance, proposed that hybrid Weyl semimetals with Weyl pairs and elongated arc-shaped TSSs can exhibit excellent catalytic performance for the HER process. For clarity, Fig. 1(a) illustrates the design scheme depicting momentum space and surface DOSs for Weyl semimetals with a pair of Weyl points [22]. On the (001) plane, a finite length of arc-shaped TSS [30–36] emerges, as shown in Fig. 1(a). However, the related catalytic activities may be comparatively weaker than those of nodal-line semimetals. Nodal-line semimetals, such as TiSi-type materials [22], featuring a single nodal line, have been reported as potential high-performance TQCs for HER. Li *et al.* [22] suggested that

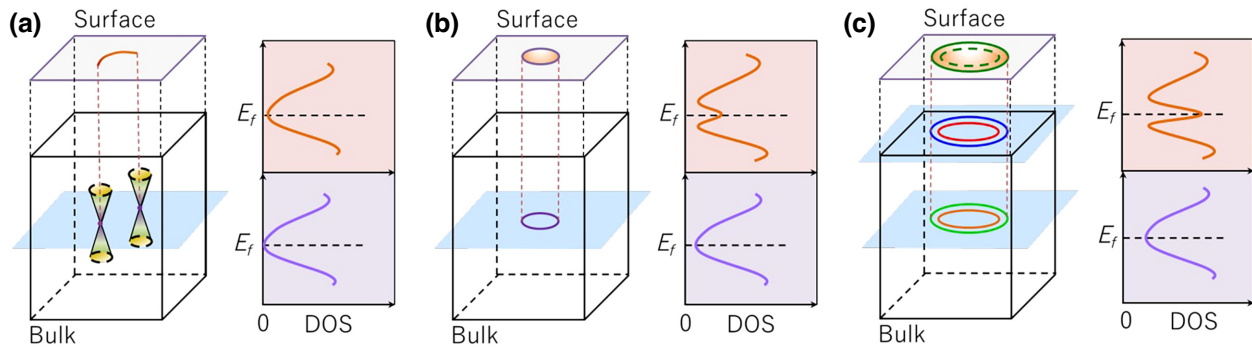


FIG. 1. The design scheme of momentum space and surface DOSs for Weyl semimetals with a pair of Weyl points, single nodal-line semimetals, and DDNL semimetals. (a) A Weyl pair in bulk and the arc-shaped TSSs on the (001) plane (left panel). (b) Single nodal line in bulk and the drumheadlike TSSs on the (001) plane (left panel). (c) DDNL in bulk (left lower panel) and multiple drumheadlike TSSs on the (001) plane (left panel). The momentum space and surface DOSs corresponding to all cases is on the right panels of (a)–(c). Note that the schematics in (a),(b) were first proposed by Li *et al.* in Ref. [22]. Here, we reproduced the schematics of (a),(b) with permission from Ref. [22]. Copyright 2017 Science China Press and Springer-Verlag GmbH Germany.

the carrier density on the surface at Fermi energy limits TQCs with Weyl pairs. They hypothesized that single nodal-line semimetals with nontrivial drumheadlike TSSs [37–39] would overcome this limitation due to the abnormally high carrier density on their surfaces near the Fermi level. Figure 1(b) depicts the design scheme illustrating the momentum space and surface DOSs for topological semimetals with a single nodal line (in the  $k_z = 0$  plane) to provide clarity. It is evident that the nodal line induces drumheadlike TSSs in the (001) plane, characterized by high surface DOSs on the (001) plane at the Fermi level [see the peak in Fig. 1(b)]. Generally, significant surface DOSs have a propensity to generate high conductivity, thereby influencing the catalytic activity for HER.

In our previous work [27], a compound NaAlGe [28] was reported to possess topological DDNLs and multiple drumheadlike TSSs. Figure 1(c) depicts the design scheme for momentum space and surface DOSs for DDNL semimetal with four nodal lines (two nodal lines in the  $k_z = 0$  plane and the other two nodal lines in the  $k_z = \pi$  plane). In comparison to the case of a single nodal line, the presence of DDNLs (multiple nodal lines) in the bulk phase results in multiple drumheadlike TSSs and associated extra high surface DOSs of the Fermi level in the (001) plane, thereby enhancing more significant catalytic activity for HER. For clarity, in Figs. 1(b) and 1(c), the peaks represent the surface DOSs of the Fermi level on the (001) plane for the single nodal-line semimetals and DDNL semimetals, respectively. In principle, the peak for DDNL semimetals is more pronounced than that for single nodal-line semimetals.

In the following section, taking NaAlGe as a representative example, we will showcase how DDNL semimetals can serve as an ideal platform for designing high-performance TQCs with abundant surface DOSs and fair-low Gibbs free energies for HER. In addition, we have successfully established a linear correlation between Gibbs free energies and surface DOSs in DDNL semimetal NaAlGe. This offers compelling evidence linking enhanced catalytic performance to surface DOSs and paves the way for developing an alternative class of high-performance catalysts from a topological perspective.

### III. RESULTS AND DISCUSSION

#### A. Band structure and surface states of NaAlGe

The NaAlGe compound has a tetragonal anti-PbFCl type structure with the  $P4/nmm$  (No. 129) space group [see Fig. 2(a)]. In this structure, one Al atom and four Ge atoms are bonded together, forming a slightly distorted diamond-like structure with Ge-Al and Na layers arranged along the  $c$ -axis cycle. The Na, Al, and Ge atoms occupy the  $2c$  (0.5, 0, 0.639),  $2c$  (0, 0, 0), and  $2a$  (0.5, 0, 0.215) Wyckoff sites within the lattice, respectively. The optimized lattice parameters of the NaAlGe compound are  $a = b = 4.168 \text{ \AA}$

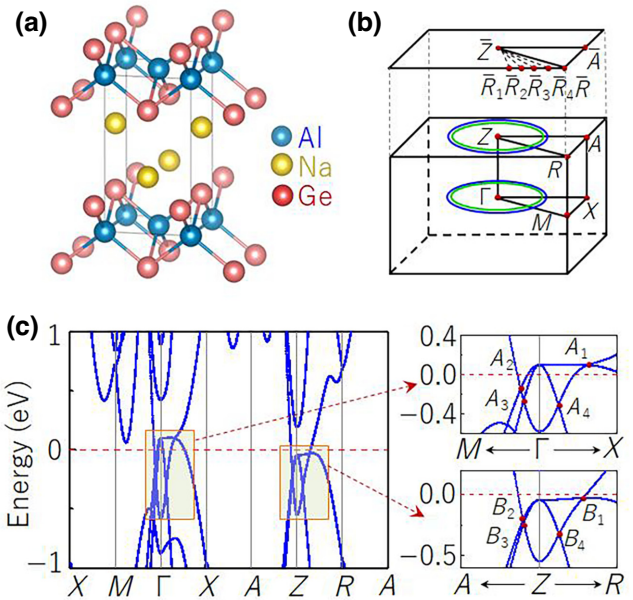


FIG. 2. (a) Crystal structure of the NaAlGe compound. (b) 3D bulk Brillouin zone and projected (001) surface. The schematic diagrams of DDNLs, i.e., two nodal lines in the  $k_z = 0$  plane and the other two nodal lines in the  $k_z = \pi$  plane, are exhibited. (c) Band structure of NaAlGe. Local enlarged figures of the bands around the Fermi level are also shown in (c), in which eight crossing points ( $A_1$ - $A_4$  and  $B_1$ - $B_4$ ) are obvious.

and  $c = 7.470 \text{ \AA}$  (match well with the previous experimental results  $a = b = 4.164 \text{ \AA}$  and  $c = 7.427 \text{ \AA}$  [28]), which are utilized in subsequent calculations.

The calculated band structure of the NaAlGe compound is shown in Fig. 2(c). Upon initial examination, a distinct semimetallic electronic structure with eight crossing points near the Fermi level is observed. These eight crossing points are not independent; instead, they form part of four concentric nodal lines. Specifically, two nodal lines are situated in the  $k_z = 0$  plane, while the other two are in the  $k_z = \pi$  plane. Figure 2(b) displays schematic diagrams of the two nodal lines centered around the  $\Gamma$  point and the two centered around the  $Z$  point, forming a DDNL system.

The projected spectra along the  $\bar{A} - \bar{Z} - \bar{R} - \bar{A}$  surface paths on the (001) surface of NaAlGe are exhibited in Fig. 3(a). Figure 3(a) illustrates multiple drumheadlike TSSs (marked by green arrows) originating from the projections of the crossing points (white balls). To verify that the drumheadlike TSSs around the Fermi level cover the entire (001) surface Brillouin zone, the projected spectra along the other surface paths on the (001) surface, including  $\bar{A} - \bar{Z} - \bar{R}_1$ ,  $\bar{A} - \bar{Z} - \bar{R}_2$ ,  $\bar{A} - \bar{Z} - \bar{R}_3$ , and  $\bar{A} - \bar{Z} - \bar{R}_4$ , are shown in Fig. 3(b). Figure 3(b) demonstrates that the ubiquitous drumheadlike TSSs around the Fermi level on the (001) surface, which lead to peaks in the surface DOSs around the Fermi level in the (001) surface for NaAlGe [see Fig. 3(a)]. For NaAlGe, the peak

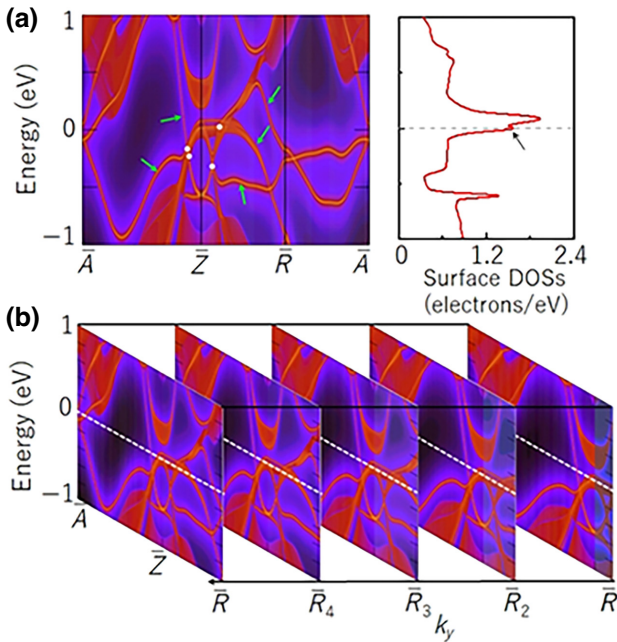


FIG. 3. (a) Projected spectrum along the  $\bar{A} - \bar{Z} - \bar{R} - \bar{A}$  surface paths and the surface DOSs on the (001) surface for NaAlGe. The drumheadlike TSSs are marked by green arrows, and the surface DOSs of the Fermi level are marked by a black arrow. (b) The evolution of the surface spectra of NaAlGe on the (001) surface by decreasing the  $k_y$  value, i.e., from  $\bar{A} - \bar{Z} - \bar{R}$  to  $\bar{A} - \bar{Z} - \bar{R}_1$  surface paths [see Fig. 2(b)].

value of the surface DOSs of the Fermi level is 1.56. In principle, due to the appearance of multiple drumheadlike TSSs induced by the DDNLs, the surface DOSs in DDNL semimetals is expected to be more significant compared to Weyl semimetals with a pair of Weyl points and single nodal-line semimetals (see Fig. 1 for details). With this in mind, one can anticipate that DDNL semimetals as TQCs may process an abnormally active and highly conductive surface and superior catalytic performance than Weyl and single nodal-line semimetals. In the following, we proceed to investigate the correlation between catalytic performance for HER and surface DOSs in NaAlGe.

## B. The relationship between catalytic performance and surface DOSs in NaAlGe

As it is known, the alignment of energy levels is one of the influential factors affecting HER activity. In Fig. 4(a), we illustrate that the energy difference between the Fermi level ( $-4.58$  eV) and the standard redox potential ( $-4.44$  eV) of the HER is quite small for NaAlGe, with a value of 0.14 eV. For the standard redox potential, we use the International Union of Pure and Applied Chemistry (IUPAC) [47] recommended experimental value of  $-4.44$  eV. This small energy difference results in a low

overpotential, which facilitates the HER process by promoting the exchange of electrons at the catalyst-electrolyte interface.

Furthermore, we examine the conditions for hydrogen diffusion on the surface of NaAlGe during the HER processes. We consider two potential mechanisms, the Tafel-step and Heyrovsky-step reactions, as shown in Fig. 4(b). We employ the climbing image-nudged elastic band (CI-NEB) method to calculate the reaction potential for hydrogen release. The results are shown in Fig. 4(b). The figure shows that the high barriers associated with the Heyrovsky-step reaction in NaAlGe are lower than those of the Tafel-step reaction. This suggests that the Volmer-Heyrovsky mechanism is dominant in HER.

Using the computational hydrogen electrode (CHE) method, initially developed by Norskov *et al.* [40], we calculate the Gibbs free energy  $\Delta G_{H^*}$  on the (001) surface of NaAlGe, which is a crucial parameter in determining the catalytic activity of HER. From Fig. 4(c), one finds the  $|\Delta G_{H^*}|$  value for NaAlGe is 0.02 eV, which is significantly lower than those of the Weyl semimetals such as NbAs (0.96 eV), TaAs (0.74 eV), TaP (0.38 eV), and NbP (0.31 eV) [17]. Furthermore, it is also lower than those of single nodal-line semimetals like TiSi (0.06 eV) [22], and PtSn<sub>4</sub> (0.11 eV) [19]. Remarkably, NaAlGe is situated at the peak of the HER volcano curve, surpassing the catalytic performance of the noble metal Pt [41]. For clarity, we also calculated the charge-density difference, showing the charge transfer during catalysis. As shown in Fig. 4(d), the charge depletion of NaAlGe occurs around the Al atom (yellow region), while charge accumulation occurs on the H atom (blue region).

In order to gain further insights into the relationship between surface DOSs and the catalytic performance for HER, we calculated  $|\Delta G_{H^*}|$  and surface DOSs of the Fermi level on various crystallographic planes, namely (010), (101), (110), (210), and (310), as illustrated in Fig. 4(e). Remarkably, the results reveal a notable linear relationship between the  $|\Delta G_{H^*}|$  and surface DOSs on different planes. Specifically, as the surface DOSs increase, the  $|\Delta G_{H^*}|$  decrease, indicating a higher catalytic activity for HER. These findings directly validate the significant contribution of surface DOSs to the observed HER performance.

To further validate the linear relationship between the  $|\Delta G_{H^*}|$  and surface DOSs in NaAlGe, we employed the electron-hole doping method to artificially modify the number of electrons (Nelec.) in the compound. This approach ensured the presence of DDNLs and effectively adjusted the energy-level position in NaAlGe. When doped with 1 or 0.5 holes (Nelec. = 15/15.5), the DDNLs on the  $k_z = 0$  and  $k_z = \pi$  planes of NaAlGe shifted away from the Fermi level. Conversely, when doped with 1 or 0.5 electrons (Nelec. = 17/16.5), the DDNLs moved downwards, distancing themselves from the Fermi level.

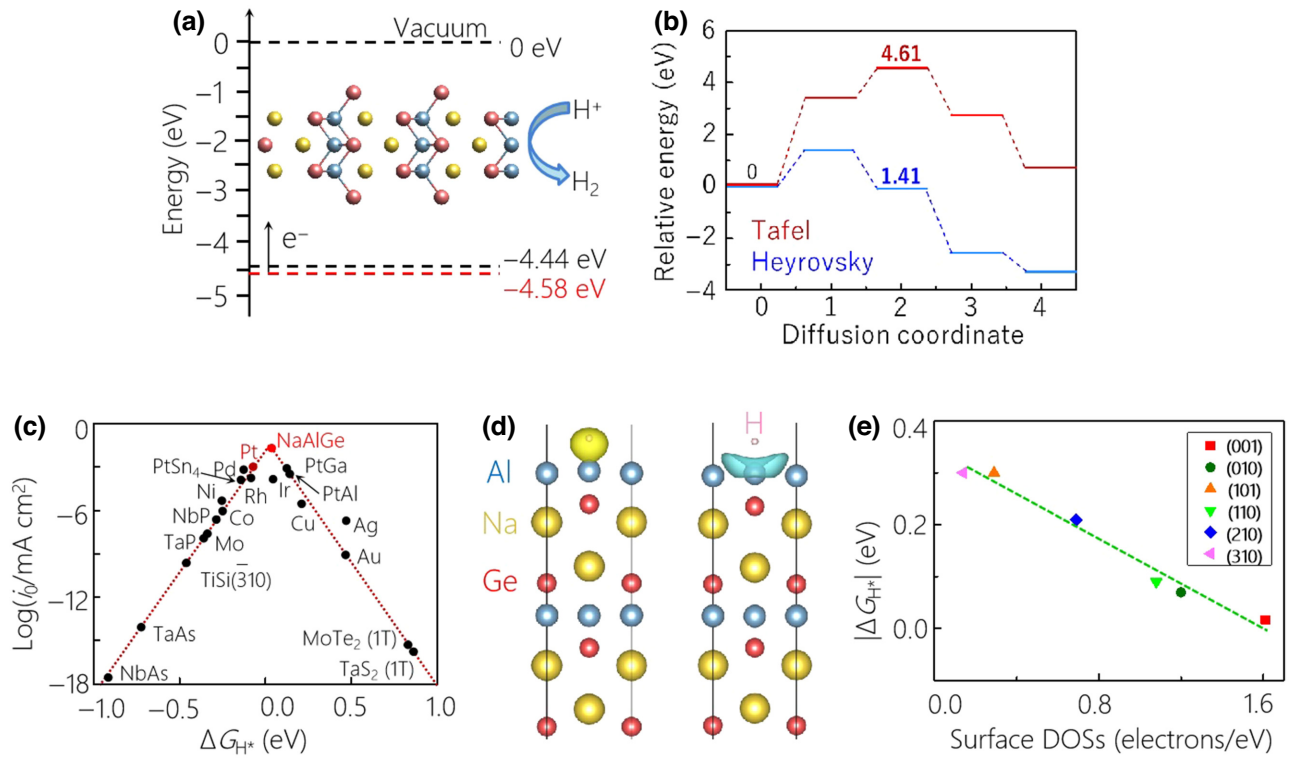


FIG. 4. (a) The energy difference between the Fermi level corresponding to the vacuum and the standard redox potential of HER for NaAlGe. (b) Reaction pathway diagram of NaAlGe on the (001) surface, including Tafel-step and Heyrovsky-step reactions. (c) Volcano plot for  $\Delta G_{H^*}$  of the NaAlGe with that of various pure metals and typical topological catalysts. The data are taken from the literature [17,22,41–45]. The calculated  $\Delta G_{H^*}$  of Pt has a value of  $-0.08$  eV, which is almost the same as that reported in the literature ( $-0.09$  eV in Ref. [46]). (d) The electron depletion (the left panel) and accumulation (the right panel) during H adsorption of NaAlGe. (e) The relationship between  $|\Delta G_{H^*}|$  and the surface DOSs of the Fermi level on different surfaces [(001), (010), (101), (110), (210), and (310)] for NaAlGe.

For clarity, Fig. 5(a) depicts the band structures of the NaAlGe with different values of Nelec., including 15, 16, and 17. Furthermore, we calculated the surface DOSs of the Fermi level for the (001) surface under various electron-hole doping conditions, as shown in Fig. 5(b). In the presence of electron-hole doping, the DDNLs move away from the Fermi level, decreasing the surface DOSs at the Fermi level. Interestingly, as shown in Fig. 5(c), we observed a linear relationship between  $|\Delta G_{H^*}|$  and surface DOSs for NaAlGe under different electron-hole doping conditions, further establishing the role of surface DOSs in catalytic activity for HER. From Fig. 5(c), for various electron-hole doping conditions, it is evident that an increase in surface DOSs of the Fermi level corresponds to a decrease in  $|\Delta G_{H^*}|$ . Remarkably, even with the various electron-hole doping conditions maintaining the presence of eight crossing points (DDNLs) in NaAlGe, the  $|\Delta G_{H^*}|$  remains relatively low under 0.2 eV [see Fig. 5(a)]. This demonstrates the robust stability of catalytic activity in NaAlGe for HER, attributable to the presence of DDNLs.

Subsequently, we conducted a study to investigate the impact of breaking the DDNLs in NaAlGe and aimed to establish a linear relationship between  $|\Delta G_{H^*}|$  and surface DOSs during topological phase transitions. Initially, we applied a small biaxial compressive strain (3%) in the  $a$ - $b$  plane, where the eight crossing points, i.e., DDNLs, were preserved in both the  $k_z = 0$  and  $k_z = \pi$  planes. When applying a larger biaxial compressive strain in the  $a$ - $b$  plane, the crossing points  $B_1$ - $B_4$ , i.e., dual nodal lines on the  $k_z = \pi$  plane, are gapped. Thus, the DDNL state is transformed into the dual nodal-line state (on the  $k_z = 0$  plane) for NaAlGe. After the biaxial compressive strain continues to increase ( $> 6.5\%$ ), all eight band crossings ( $A_1$ - $A_4$  and  $B_1$ - $B_4$ ) are gapped, and the DDNL state is totally broken. The examples of band structures for NaAlGe under 0%, 3%, and 6.5% biaxial compressive strains are shown in Fig. 6(a). From Fig. 6(b), one finds that the surface DOSs of the Fermi level progressively decreases with increasing biaxial compressive strains. Moreover, Fig. 6(c) demonstrates a well-established linear relationship between  $|\Delta G_{H^*}|$  and surface DOSs for various

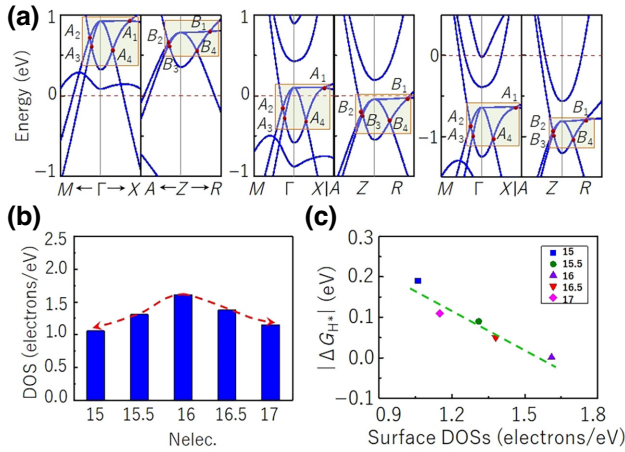


FIG. 5. (a) Calculated band structures for NaAlGe with Nelec. = 15, Nelec. = 16, and Nelec. = 17, respectively. (b) The calculated surface DOSs of the Fermi level for NaAlGe with different values of Nelec. (c) The linear relationship between  $|\Delta G_{H^*}|$  and the surface DOSs for NaAlGe with varying values of Nelec.

biaxial compressive strains, indicating the effectiveness of surface DOSs in enhancing the catalytic activity for HER. For biaxial compressive strains below 3%, the  $|\Delta G_{H^*}|$  tends to increase as the area of the double DDNLs on both planes decreases. Nevertheless, the DDNLs in NaAlGe are maintained, resulting in a low  $|\Delta G_{H^*}|$  value ( $< 0.2$  eV) and sustained HER activity. When a 5% biaxial compression strain is applied, only the dual nodal lines persist in the  $k_z = 0$  plane, leading to a sharp increase in  $|\Delta G_{H^*}|$  and a decline in HER activity. Furthermore, by further disrupting

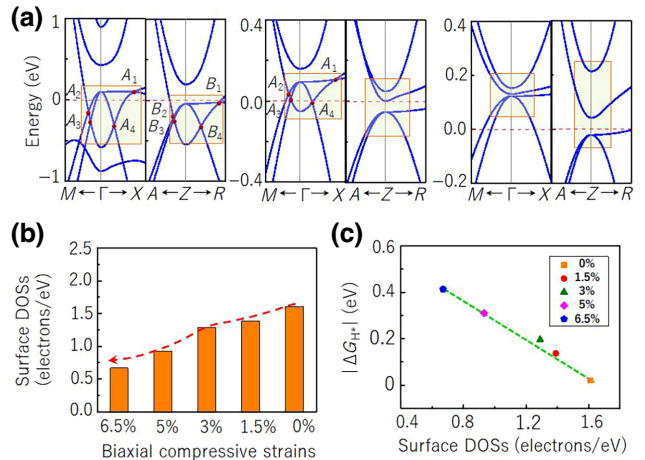


FIG. 6. (a) Calculated band structures for NaAlGe under 0%, 3%, and 6.5% biaxial compressive strains, respectively. (b) The calculated surface DOSs of the Fermi level for NaAlGe under different biaxial compressive strains. (c) The linear relationship between  $|\Delta G_{H^*}|$  and the surface DOSs for NaAlGe under different biaxial compressive strains.

the dual nodal lines in the  $k_z = 0$  plane by applying a 6.5% biaxial compressive strain, the  $|\Delta G_{H^*}|$  has a further sharp increase, significantly weakening the HER activity. It is worthwhile to note that these findings strongly support the hypothesis presented in Fig. 1.

### C. Other promising TQCs with DDNLs

In our pursuit to identify other promising TQCs with DDNLs, we conducted a comprehensive screening using

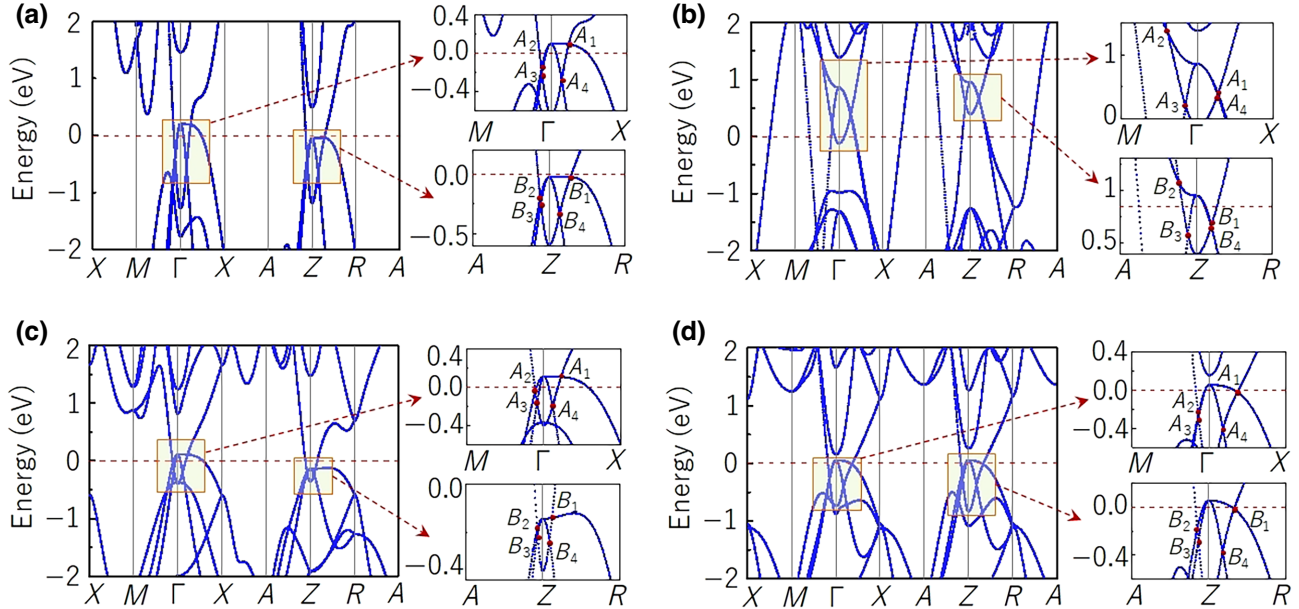


FIG. 7. (a)-(d) Band structures for NaAlSi, ErSe<sub>2</sub>, NaZnSb, and BaAlGeF, respectively. The orange frame region highlights the DDNLs.

the Materials Project database [48]. The ideal TQCs with DDNLs must satisfy the following requirements: (i) the DDNLs should be located in close proximity to the Fermi level; (ii) there should be no interfering bands in the vicinity of the DDNLs; and (iii) the calculated  $|\Delta G_{H^*}|$  should be close to zero.

As a result of our screening, we discovered four other TQCs with favorable DDNL characteristics: NaAlSi [49], ErSe<sub>2</sub> [50], NaZnSb [51], and BaAlGeF. The calculated band structures for NaAlSi, ErSe<sub>2</sub>, NaZnSb, and BaAlGeF are shown in Fig. 7. The eight crossing points, which belong to the DDNLs, appear around the Fermi level.

We calculate the Gibbs free energy  $\Delta G_{H^*}$  on the (001) surface of NaAlSi, ErSe<sub>2</sub>, NaZnSb, and BaAlGeF, which is a crucial parameter in determining the catalytic activity of HER. Figure 8 presents the calculated values of  $|\Delta G_{H^*}|$  for these four materials, all of which are below 0.15 eV. The  $|\Delta G_{H^*}|$  values for NaAlSi, ErSe<sub>2</sub>, NaZnSb, and BaAlGeF are 0.03, 0.05, 0.10, and 0.12 eV, respectively. We also calculated the charge-density differences of NaAlSi, ErSe<sub>2</sub>, NaZnSb, and BaAlGeF, as shown in Fig. 9, which shows the charge transfer during catalysis.

Notably, NaAlGe and NaAlSi exhibit  $|\Delta G_{H^*}|$  values close to 0, indicating an exceptionally high HER activity. Moreover, Fig. 8 shows that the  $|\Delta G_{H^*}|$  is linearly correlated with the projected surface DOSs on the (001) semi-infinite surface for the NaAlSi, NaAlGe, ErSe<sub>2</sub>, NaZnSb, and BaAlGeF. Specifically, the higher the surface DOSs of the Fermi level, the lower value of  $|\Delta G_{H^*}|$ , implying stronger catalytic activity for HER.

The energy differences between the Fermi level corresponding to the vacuum and the standard redox potential of the HER standard potential for NaAlSi, ErSe<sub>2</sub>,

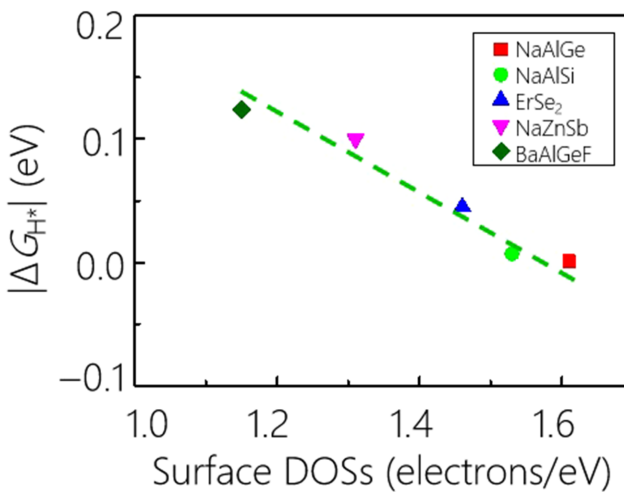


FIG. 8. A linear relationship between the  $|\Delta G_{H^*}|$  and the projected surface DOSs on the (001) semi-infinite surface for the DDNL materials.

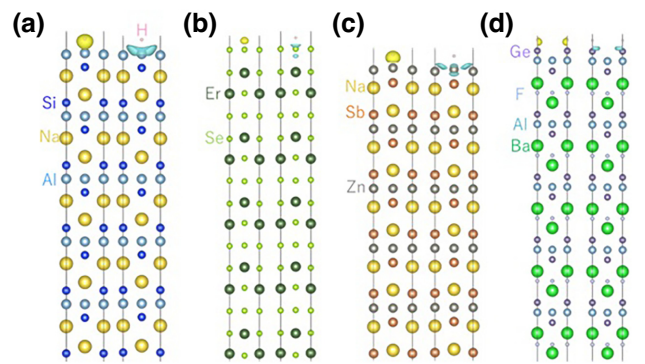


FIG. 9. (a)–(d) The electron depletion and accumulation during H adsorption of NaAlSi, ErSe<sub>2</sub>, NaZnSb, and BaAlGeF, respectively.

NaZnSb, and BaAlGeF, respectively, are shown in Fig. 10. The Fermi energy levels of NaAlSi, ErSe<sub>2</sub>, NaZnSb, and BaAlGeF are  $-4.60$ ,  $-5.49$ ,  $-4.61$ , and  $-4.08$  eV, respectively. One finds that energy differences are small ( $< 0.4$  eV) for NaAlSi, NaZnSb, and BaAlGeF, and the low overpotential benefits the HER process. These findings underscore the potential of these DDNL materials as highly active catalysts for HER, emphasizing their suitability for future exploration and application in catalysis research.

We calculated the reaction potential for hydrogen release with the help of the CI-NEB method and showed the results in Fig. 11. Figure 11 shows that the Heyrovsky-step reaction is the preferred pathway for the hydrogen release of ErSe<sub>2</sub>, NaZnSb, and BaAlGeF. However, for NaAlSi, the preferred pathway for hydrogen release is the Tafel-step reaction.

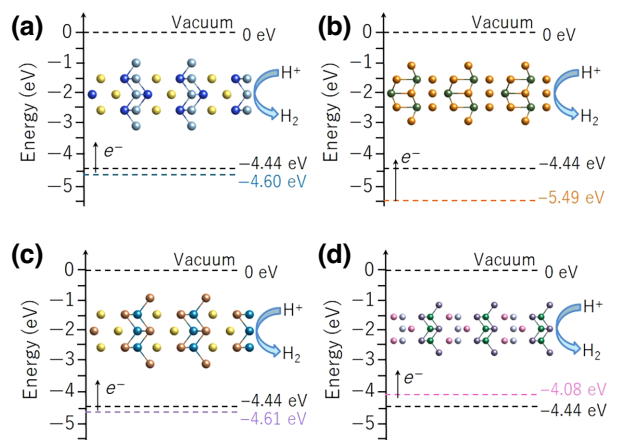


FIG. 10. (a)–(d) The energy differences between the Fermi level corresponding to the vacuum and the standard redox potential of the HER standard potential for NaAlSi, ErSe<sub>2</sub>, NaZnSb, and BaAlGeF, respectively.

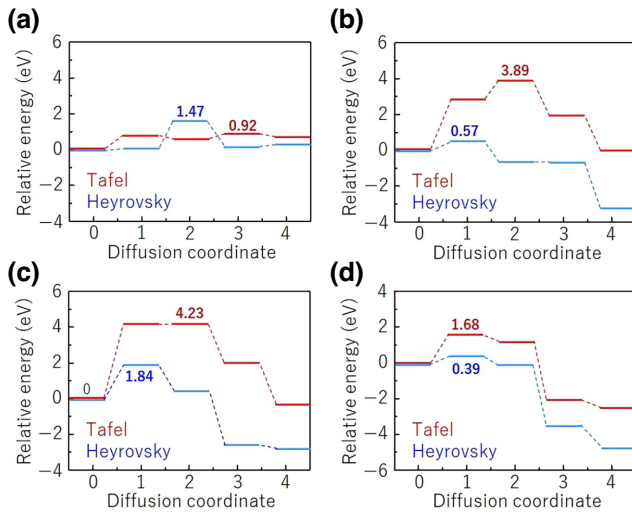


FIG. 11. (a)–(d) Reaction pathway diagrams of NaAlSi, ErSe<sub>2</sub>, NaZnSb, and BaAlGeF on the (001) surface, including Tafel-step and Heyrovsky-step reactions.

#### IV. CONCLUSION AND REMARKS

In summary, our study demonstrates the potential of DDNL semimetals with large topological surface DOSs as highly active surface TQCs. Using an experimentally prepared NaAlGe compound as an example, we find its DDNLs around the Fermi level will induce ubiquitous drumheadlike TSSs on the (001) surface, resulting in high surface DOSs around the Fermi level and further enhancing the electron transfer capability and the catalytic performance for HER. Notably, the  $|\Delta G_{\text{H}^*}|$  of NaAlGe approaches zero, even comparable to Pt, positioning it near the summit of the volcano diagram. More interestingly, we establish a linear relationship between the  $|\Delta G_{\text{H}^*}|$  and surface DOSs for NaAlGe across different surfaces, electron-hole doping conditions, and biaxial compressive strains. It is well documented that surface DOSs around the Fermi level contribute to increased catalytic activity for HER. With these findings, we anticipate that our work will pave the way for the development of high-performance catalysts based on the DDNL semimetals exhibiting high surface DOSs.

In this work, we demonstrate that DDNL semimetals with higher surface DOSs than previously postulated TQCs, including Weyl semimetals and single nodal-line semimetals, can be an ideal HER platform. Our work quantificationally linked the catalytic activity and topological state of matter in TQCs with DDNLs. That is, this work discovers the linear correlations between the catalytic activity for HER and the projected topological surface DOSs on corresponding surfaces, providing direct evidence that the catalytic enhancement is indeed from the surface states in the DDNL semimetals. The discovery of these linear correlations will open another route for

developing high-performance catalysts from the quantum topological point of view. Furthermore, the established linear correlations facilitate the understanding of complicated electrochemical processes for topological catalyst design.

#### V. METHODS

All the first-principles calculations in this work use the Vienna *ab initio* simulation package (VASP) [52] within the framework of density-functional theory (DFT) [53]. The exchange-correlation potential made use of the generalized gradient approximation (GGA) [54] of the Perdew-Burke-Ernzerhof (PBE) method [55]. A cutoff energy of 500 eV was adopted. The convergence criterion for the residual force and energy was set to 0.01 eV/Å and  $10^{-4}$  eV. The Brillouin zones (BZs) were sampled by  $\Gamma$ -centered  $k$ -point mesh with a  $13 \times 13 \times 7$   $k$ -point grid for calculation of band structure and  $5 \times 5 \times 1$  for structure optimization of slab model. The Slab model used 20-Å vacuum layers to avoid the interaction between layers. The DFT-D2 method was adopted to consider long-range van der Waals interaction. The calculation of surface DOSs of all materials requires the use of the maximum localization Wannier function [56,57] and the WannierTools package [58].

$\Delta G_{\text{H}^*}$  is defined as

$$\Delta G_{\text{H}^*} = \Delta E_{\text{H}} + \Delta E_{\text{ZPE}} - T\Delta S_{\text{H}}. \quad (1)$$

$\Delta E_{\text{H}}$  is the adsorption energy of hydrogen on the substrate, which is defined as

$$\Delta E_{\text{H}} = \frac{1}{n} \left( E_{\text{NaAlGe+H}} - E_{\text{NaAlGe}} - \frac{2}{n} E_{\text{H}_2} \right), \quad (2)$$

where  $n$  is the number of hydrogens.  $E_{\text{NaAlGe+H}}$  and  $E_{\text{NaAlGe}}$  are expressed as the total energy of the adsorption system and the total energy of the substrate, respectively.  $E_{\text{H}_2}$  is the total energy of the hydrogen molecule.  $\Delta E_{\text{ZPE}}$  [43] refers to the zero-point energy difference between adsorbed and gaseous hydrogen. The  $\Delta E_{\text{ZPE}}$  value calculated is close to 0 eV in this work. The surface temperature ( $T$ ) is taken as room temperature  $T = 300$  K. The entropy change ( $\Delta S_{\text{H}}$ ) [59,60] is given by

$$\Delta S_{\text{H}} = \frac{1}{2} S_{\text{H}_2}^0 \quad (3)$$

$S_{\text{H}_2}^0$  is the entropy of hydrogen under standard conditions of 130.684 J/(K mol) with considering the small vibrational entropy of adsorbed hydrogen. Equation (3) can therefore be simplified as  $S_{\text{H}} \approx 0.22$  eV. Based on the above, Eq. (1) can be simplified as

$$\Delta G_{\text{H}^*} = \Delta E_{\text{H}} + 0.22 \text{ eV}. \quad (4)$$

## ACKNOWLEDGMENTS

This paper was supported by the National Key R&D Program of China (Grant No. 22022YFA1402600), the Overseas Scientists Sponsorship Program by Hebei Province (Grant No. C20230502), and the National Natural Science Foundation of China (Grant No. 12274112).

- 
- [1] J. A. Turner, Sustainable hydrogen production, *Science* **305**, 5686 (2004).
- [2] X. Wang, K. Maeda, A. Thomas, K. Takanabe, G. Xin, J. M. Carlsson, K. Domen, and M. Antonietti, A metal-free polymeric photocatalyst for hydrogen production from water under visible light, *Nat. Mater.* **8**, 76 (2009).
- [3] J. Mahmood, M. A. R. Anjum, S. H. Shin, I. Ahmad, H. J. Noh, S. J. Kim, H. Y. Jeong, J. S. Lee, and J. B. Baek, Encapsulating iridium nanoparticles inside a 3D cage-like organic network as an efficient and durable catalyst for the hydrogen evolution reaction, *Adv. Mater.* **30**, 1805606 (2018).
- [4] J. Zhang, K. Sasaki, E. Sutter, and R. Adzic, Stabilization of platinum oxygen-reduction electrocatalysts using gold clusters, *Science* **315**, 220 (2007).
- [5] R. Subbaraman, D. Tripkovic, D. Strmcnik, K. C. Chang, M. Uchimura, A. P. Paulikas, V. Stamenkovic, and N. M. Markovic, Enhancing hydrogen evolution activity in water splitting by tailoring  $\text{Li}^+ - \text{Ni(OH)}_2\text{-Pt}$  interfaces, *Science* **334**, 1256 (2011).
- [6] G. Chen, T. Wang, J. Zhang, P. Liu, H. Sun, X. Zhuang, M. Chen, and X. Feng, Accelerated hydrogen evolution kinetics on NiFe-layered double hydroxide electrocatalysts by tailoring water dissociation active sites, *Adv. Mater.* **30**, 1706279 (2018).
- [7] M. F. Li, *et al.*, Single-atom tailoring of platinum nanocatalysts for high-performance multifunctional electrocatalysis, *Nat. Catal.* **2**, 495 (2019).
- [8] M. Kuang, Q. Wang, P. Han, and G. Zheng, Cu, Co-embedded N-enriched mesoporous carbon for efficient oxygen reduction and hydrogen evolution reactions, *Adv. Energy Mater.* **7**, 1700193 (2017).
- [9] G. Zhao, K. Rui, S. X. Dou, and W. Sun, Heterostructures for electrochemical hydrogen evolution reaction: a review, *Adv. Funct. Mater.* **28**, 1803291 (2018).
- [10] J. N. Tiwari, S. Sultan, C. W. Myung, T. Yoon, N. N. Li, M. R. Ha, A. M. Harzandi, H. J. Park, D. Y. Kim, S. S. Chandrasekaran, W. G. Lee, V. Vij, H. J. Kang, T. J. Shin, H. S. Shin, G. Lee, Z. Lee, and K. S. Kim, Multicomponent electrocatalyst with ultralow Pt loading and high hydrogen evolution activity, *Nat. Energy* **3**, 773 (2018).
- [11] N. C. Cheng, S. Stambula, D. Wang, M. N. Banis, J. Liu, A. Riese, B. W. Xiao, R. Y. Li, T.-K. Sham, L.-M. Liu, G. L. G. A. Botton, and X. L. Sun, Platinum single-atom and cluster catalysis of the hydrogen evolution reaction, *Nat. Commun.* **7**, 13638 (2016).
- [12] H. Luo, P. Yu, G. Li, and K. Yan, Topological quantum materials for energy conversion and storage, *Nat. Rev. Phys.* **4**, 611 (2022).
- [13] L. Wang, Y. Yang, J. Wang, W. Liu, Y. Liu, J. Gong, G. Liu, X. Wang, Z. Cheng, and X. Zhang, Excellent catalytic performance toward the hydrogen evolution reaction in topological semimetals, *EcoMat* **5**, e12316 (2023).
- [14] H. Chen, W. Zhu, D. Xiao, and Z. Zhang, CO oxidation facilitated by robust surface states on Au-covered topological insulators, *Phys. Rev. Lett.* **107**, 056804 (2011).
- [15] J. Xiao, L. Kou, C. Y. Yam, T. Frauenheim, and B. Yan, Toward rational design of catalysts supported on a topological insulator substrate, *ACS Catal.* **5**, 7063 (2015).
- [16] L. Li, J. Zeng, W. Qin, P. Cui, and Z. Zhang, Tuning the hydrogen activation reactivity on topological insulator heterostructures, *Nano Energy* **58**, 40 (2019).
- [17] C. R. Rajamathi, U. Gupta, N. Kumar, H. Yang, Y. Sun, V. Süß, C. Shekhar, M. Schmidt, H. Blumtritt, P. Werner, B. Yan, S. Parkin, C. Felser, and C. N. R. Rao, Weyl semimetals as hydrogen evolution catalysts, *Adv. Mater.* **29**, 1606202 (2017).
- [18] D. Lu, X. Ren, L. Ren, W. Xue, S. Liu, Y. Liu, Q. Chen, X. Qi, and J. Zhong, Direct vapor deposition growth of 1T'  $\text{MoTe}_2$  on carbon cloth for electrocatalytic hydrogen evolution, *ACS Appl. Energy Mater.* **3**, 3212 (2019).
- [19] G. Li, *et al.*, Dirac nodal arc semimetal  $\text{PtSn}_4$ : An ideal platform for understanding surface properties and catalysis for hydrogen evolution, *Angew. Chem.* **131**, 13241 (2019).
- [20] Q. Yang, G. Li, K. Manna, F. Fan, C. Felser, and Y. Sun, Topological engineering of Pt-group-metal-based chiral crystals toward high-efficiency hydrogen evolution catalysts, *Adv. Mater.* **32**, 1908518 (2020).
- [21] W. Meng, X. Zhang, Y. Liu, X. Dai, G. Liu, Y. Gu, E. P. Kenny, and L. Kou, Multifold fermions and Fermi arcs boosted catalysis in nanoporous electride  $12\text{CaO} \cdot 7\text{Al}_2\text{O}_3$ , *Adv. Sci.* **10**, 2205940 (2023).
- [22] J. Li, H. Ma, S. Feng, S. Ullah, R. Li, J. Dong, D. Li, Y. Li, and X.-Q. Chen, Topological quantum catalyst: Dirac nodal line states and a potential electrocatalyst of hydrogen evolution in the TiSi family, *Sci. China Mater.* **61**, 23 (2018).
- [23] X. Zhang, L. Wang, M. Li, W. Meng, Y. Liu, X. Dai, G. Liu, Y. Gu, J. Liu, and L. Kou, Topological surface state: Universal catalytic descriptor in topological catalysis, *Mater. Today* **67**, 23 (2023).
- [24] Q. Xu, G. Li, Y. Z. Q. Yang, Y. Sun, and C. Felser, Descriptor for hydrogen evolution catalysts based on the bulk band structure effect, *ACS Catal.* **10**, 5042 (2020).
- [25] Z. Gao, F. Ma, H. Wu, Y. Ge, Z. Zhu, Y. Liu, Y. Jiao, and Z. Chen, Two-dimensional ruthenium boride: a Dirac nodal loop quantum electrocatalyst for efficient hydrogen evolution reaction, *J. Mater. Chem. A* **11**, 3717 (2023).
- [26] X. Yi, W. Q. Li, Z. H. Li, P. Zhou, Z. S. Ma, and L. Z. Sun, Topological dual double node-line semimetals  $\text{NaAlSi}$  (Ge) and their potential as cathode material for sodium ion batteries, *J. Mater. Chem. C* **7**, 15375 (2019).
- [27] X. Wang, G. Ding, Z. Cheng, G. Surucu, X.-L. Wang, and T. Yang, Rich topological nodal line bulk states together with drum-head-like surface states in  $\text{NaAlGe}$  with anti-PbFCl type structure, *J. Adv. Res.* **23**, 95 (2020).
- [28] Z. Chen, Y. Yang, J. Deng, T. Ying, J. Guo, and X. L. Chen, Delicate superconductivity in nodal-line  $\text{NaAlGe}$  single crystal, *J. Phys.: Condens. Matter* **34**, 495702 (2022).

- [29] W. Liu, X. M. Zhang, W. Z. Meng, Y. Liu, X. F. Dai, and G. D. Liu, Theoretical realization of hybrid Weyl state and associated high catalytic performance for hydrogen evolution in NiSi, *iScience* **25**, 103543 (2022).
- [30] S.-Y. Xu, C. Liu, S. K. Kushwaha, R. Sankar, J. W. Krizan, I. Belopolski, M. Neupane, G. Bian, N. Alidoust, T.-R. Chang, H.-T. Jeng, C.-Y. Huang, W.-F. Tsai, H. Lin, P. P. Shibayev, F.-C. Chou, R. J. Cava, and M. Z. Hasan, Observation of Fermi arc surface states in a topological metal, *Science* **347**, 294 (2015).
- [31] Z. P. Wang, Z. P. Li, Y. L. Wang, S. J. Shen, Q. S. Zhang, J. C. Wang, and W. W. Zhong, Nontrivial topological surface states in  $\text{Ru}_3\text{Sn}_7$  toward wide pH-range hydrogen evolution reaction, *Adv. Mater.* **35**, 2302007 (2023).
- [32] S.-Y. Xu, *et al.*, Discovery of a Weyl fermion semimetal and topological Fermi arcs, *Science* **349**, 613 (2015).
- [33] X. Wang, T. Yang, Z. Cheng, G. Surucu, J. Wang, F. Zhou, Z. Zhang, and G. Zhang, Topological nodal line phonons: Recent advances in materials realization, *Appl. Phys. Rev.* **9**, 041304 (2022).
- [34] G. Ding, C. Xie, J. Bai, Z. Cheng, X. Wang, and W. Wu, Recipe for single-pair-Weyl-points phonons carrying the same chiral charges, *Phys. Rev. B* **108**, L020302 (2023).
- [35] G. Ding, C. Xie, J. Gong, J. Wang, J. Bai, W. Wang, D. Li, X.-P. Li, and Xiaotian Wang, Exotic topological phonon modes in semiconductors: Symmetry analysis and first-principles calculations for representative examples, *Phys. Rev. B* **108**, 075201 (2023).
- [36] J. Li, Y. Liu, J. Bai, C. Xie, H. Yuan, Z. Cheng, W. Wang, X. Wang, and G. Zhang, Phononic Weyl pair, phononic Weyl complex, phononic real Chern insulator state, and phononic corner modes in 2D Kekule-order graphene, *Appl. Phys. Rev.* **10**, 031416 (2023).
- [37] I. Belopolski, *et al.*, Discovery of topological Weyl fermion lines and drumhead surface states in a room temperature magnet, *Science* **365**, 1278 (2019).
- [38] W. Deng, J. Lu, F. Li, X. Huang, M. Yan, J. Ma, and Z. Liu, Nodal rings and drumhead surface states in phononic crystals, *Nat. Commun.* **10**, 1769 (2019).
- [39] L. Muechler, A. Topp, R. Queiroz, M. Krivenkov, A. Varykhalov, J. Cano, C. R. Ast, and L. M. Schoop, Modular arithmetic with nodal lines: Drumhead surface states in  $\text{ZrSiTe}$ , *Phys. Rev. X* **10**, 011026 (2020).
- [40] J. K. Nørskov, J. Rossmeisl, A. Logadottir, L. R. K. J. Lindqvist, J. R. Kitchin, T. Bligaard, and H. Jonsson, Origin of the overpotential for oxygen reduction at a fuel-cell cathode, *J. Phys. Chem. B* **108**, 17886 (2004).
- [41] J. Greeley, T. F. Jaramillo, J. Bonde, I. Chorkendorff, and J. K. Nørskov, Computational high-throughput screening of electrocatalytic materials for hydrogen evolution, *Nat. Mater.* **5**, 909 (2006).
- [42] C. R. Rajamathi, U. Gupta, K. Pal, N. Kumar, H. Yang, Y. Sun, C. Shekhar, B. H. Yan, S. Parkin, U. V. Waghmare, C. Felser, and C. N. R. Rao, Expediting hydrogen evolution through topological surface states on  $\text{Bi}_2\text{Te}_3$ , *ACS Catal.* **10**, 2656 (2017).
- [43] J. K. Nørskov, T. Bligaard, A. Logadottir, J. R. Kitchin, J. G. Chen, S. Pandelov, and U. Stimming, Trends in the exchange current for hydrogen evolution, *J. Electrochem. Soc.* **152**, J23 (2005).
- [44] T. F. Jaramillo, K. P. Jørgensen, J. Bonde, J. H. Nielsen, S. Horch, and I. Chorkendorff, Identification of active edge sites for electrochemical  $\text{H}_2$  evolution from  $\text{MoS}_2$  nanocatalysts, *Science* **317**, 100 (2007).
- [45] J. K. Nørskov, T. Bligaard, J. Rossmeisl, and C. H. Christensen, Towards the computational design of solid catalysts, *Nat. Chem.* **1**, 37 (2009).
- [46] Z. W. Seh, J. Kibsgaard, C. F. Dickens, I. B. Chorkendorff, J. K. Nørskov, and T. F. Jaramillo, Combining theory and experiment in electrocatalysis: Insights into materials design, *Science*, **355**, eaad4998 (2017).
- [47] S. Trasatti, Influence of the valve metal oxide on the properties of ruthenium based mixed oxide electrodes: Part I. Titanium supported  $\text{RuO}_2/\text{Ta}_2\text{O}_5$  layers, *Pure Appl. Chem.* **209**, 0022 (1986).
- [48] A. Jain, S. P. Ong, G. Hautier, W. Chen, W. D. Richards, S. Dacek, S. Cholia, D. Gunter, D. Skinner, G. Ceder, and K. A. Persson, Commentary: The Materials Project: A materials genome approach to accelerating materials innovation, *APL Mater.* **1**, 011002 (2013).
- [49] D. Hirai, T. Ikenobe, T. Yamada, H. Yamane, and Z. Hiroi, Unusual resistive transitions in the nodal-line semimetallic superconductor  $\text{NaAlSi}$ , *J. Phys. Soc. Japan* **91**, 024702 (2022).
- [50] W. W. Alan and H. T. Hall, High-pressure synthesis of rare earth polyselenides, *Inorg. Chem.* **9**, 843 (1970).
- [51] V. Gvozdetskyi, B. Owens-Baird, S. Hong, and J. V. Zaikina, Thermal stability and thermoelectric properties of  $\text{NaZnSb}$ , *Materials* **12**, 48 (2019).
- [52] G. Kresse and D. Joubert, From ultrasoft pseudopotentials to the projector augmented-wave method, *Phys. Rev. B: Condens. Matter Mater. Phys.* **59**, 1758 (1999).
- [53] J. P. Perdew, K. Burke, and M. Ernzerhof, Generalized gradient approximation made simple, *Phys. Rev. Lett.* **77**, 3865 (1996).
- [54] S. Grimme, Semiempirical GGA-type density functional constructed with a long-range dispersion correction, *J. Comput. Chem.* **27**, 1787 (2006).
- [55] A. Togo, F. Oba, and I. Tanaka, First-principles calculations of the ferroelastic transition between rutile-type and  $\text{CaCl}_2$ -type  $\text{SiO}_2$  at high pressures, *Phys. Rev. B* **78**, 134106 (2008).
- [56] N. Marzari and D. Vanderbilt, Maximally localized generalized Wannier functions for composite energy bands, *Phys. Rev. B: Condens. Matter Mater. Phys.* **56**, 12847 (1997).
- [57] A. A. Mostofi, J. R. Yates, Y.-S. Lee, I. Souza, D. Vanderbilt, and N. Marzari, wannier90: A tool for obtaining maximally-localised Wannier functions, *Comput. Phys. Commun.* **178**, 685 (2008).
- [58] Q. S. Wu, S. N. Zhang, H.-F. Song, M. Troyer, and A. A. Soluyanov, WannierTools: An open-source software package for novel topological materials, *Comput. Phys. Commun.* **224**, 405 (2018).
- [59] L. Q. Lia, J. Zeng, W. Qina, P. Cui, and Z. Y. Zhang, Tuning the hydrogen activation reactivity on topological insulator heterostructures, *Nano Energy* **58**, 40 (2019).
- [60] Y. R. An, X. L. Fan, H. J. Liu, and Z. F. Luo, Improved catalytic performance of monolayer nano-triangles  $\text{WS}_2$  and  $\text{MoS}_2$  on HER by 3d metals doping, *Comput. Mater. Sci.* **159**, 333 (2019).